

VIP Very Important Paper

Pyridinic Nitrogen-Doped Graphene Nanoshells Boost the Catalytic Efficiency of Palladium Nanoparticles for the *N*-Allylation Reaction

Xinxin Li,^[a] Qingshan Zhao,^{*[a]} Xiang Feng,^[a] Lei Pan,^[a] Zhuangzhuang Wu,^[a] Xiaocui Wu,^[a] Tianwen Ma,^[a] Jialiang Liu,^[a] Yuanyuan Pan,^[a] Yan Song,^[b] and Mingbo Wu^{*[a]}

In this study, nitrogen-doped graphene nanoshells (N-GNS) were developed to support palladium nanoparticles (Pd/N-GNS) as an efficient and recyclable catalyst for the *N*-allylation reaction. N-GNS was synthesized through a facile hard-template method by using petroleum asphalt, followed by nitrogen doping by thermal annealing with urea, the contents and species of which could be altered by the calcination temperature. Palladium nanoparticles (Pd NPs) with an average diameter of 3.3 nm were homogeneously deposited onto the N-GNS support through a mild solvent-growth approach. The Pd/N-GNS exhibited a superior activity towards the *N*-allylation reaction, 6-fold higher than that of the pristine graphene nanoshells supporting the palladium catalyst. The Pd/N-GNS could

be recycled several times without activity deterioration and metal leaching. The catalytic activity showed a linear correlation relationship with the pyridinic N content. Experimental and theoretical studies reveal strong metal-support interactions between the pyridinic N and palladium species, which can downsize the Pd NPs, modulate the electronic properties, and promote the adsorption of reactant, thereby significantly boosting the catalytic efficiency and stability for the *N*-allylation process. The present work could help unravel the roles of nitrogen-doped carbon supports and provides a feasible strategy to rationally design superior palladium catalysts for chemical transformations.

Introduction

N-Allylation reactions are one of the most powerful synthetic tools for the formation of C–N bonds; they have been recognized as an important infrastructure in organic synthesis.^[1,2] Consequently, the diverse functionalization of various allylic compounds with amines as nucleophiles has been developed for the synthesis of pharmaceuticals, natural products, and fine chemicals.^[3,4] Among the numerous catalytic species, palladium-based catalysts stand out for their high efficiency toward the C–N coupling owing to their unique coordination and activation properties.^[5] However, classic homogeneous palladium complexes with sterically demanding electron-rich phosphine or *N*-heterocyclic carbene (NHC) ancillary ligands are expensive, air sensitive, and difficult to separate from the reaction system, which seriously restricts their practical applications.^[6–8]

Thus, the development of heterogeneous palladium catalysts for *N*-allylation reactions has recently drawn much attention. Motokura et al. stabilized Pd-bisphosphine complexes on SiO₂ surfaces as a high-performance catalyst for allylation of various nucleophiles.^[9] Vittoz et al. co-entrapped palladium nanoparticles (Pd NPs) with ionic liquid inside a sodium alginate matrix as a highly active and recyclable catalyst for allylic substitution reactions.^[10] Supported palladium catalysts are readily separated and recycled through filtration or centrifugation. Unfortunately, the inferior catalytic activity and selectivity still makes developing highly efficient and recyclable palladium catalysts an urgent task.^[11–13]

Previous studies have demonstrated that the interactions between catalytic species and the support play significant roles in the catalytic activity and stability.^[14–16] Compared with other carriers [e.g., silica,^[17] zeolite,^[18] metal oxides,^[19,20] metal-organic frameworks (MOFs),^[21] etc.], carbon materials provide versatile substrates for metallic catalysts owing to their unique physicochemical properties, such as controllable morphology, high surface area, thermal and chemical stability, and the availability for chemical modifications.^[22,23] In particular, intercalating heteroatoms into carbon skeletons can further tailor the support properties and adjust the catalytic performance of the active metallic species on the support. Recently, nitrogen-doped carbon materials have been reported to be promising matrixes for Pd NPs in various chemical transformations.^[24–26] Nitrogen doping can efficiently promote the overall catalytic activity and selectivity by modifying the interactions between

[a] X. X. Li, Q. S. Zhao, X. Feng, L. Pan, Z. Z. Wu, X. C. Wu, T. W. Ma, J. L. Liu, Y. Y. Pan, M. B. Wu
State Key Laboratory of Heavy Oil Processing
Institute of New Energy, College of Chemical Engineering
China University of Petroleum (East China)
Qingdao 266580 (P.R. China)
E-mail: qszhao@upc.edu.cn
wumb@upc.edu.cn

[b] Y. Song
CAS Key Laboratory of Carbon Materials
Chinese Academy of Sciences
Taiyuan 030001 (P.R. China)

 Supporting Information and the ORCID identification number(s) for the author(s) of this article can be found under:
<https://doi.org/10.1002/cssc.201802532>

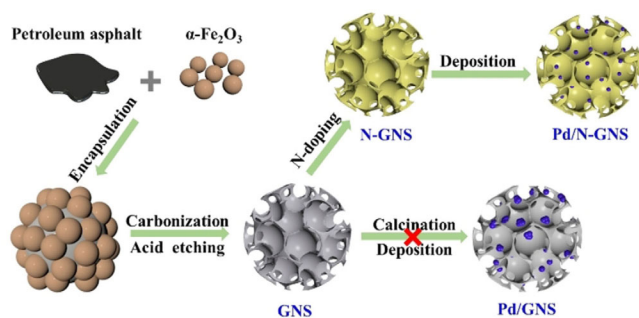
the support and palladium active species.^[27,28] For instance, Bi et al. reported that pyridinic N doped carbon supports can enhance the catalytic performance of palladium for dehydrogenation of formic acid.^[29] Koh et al. demonstrated that pyridinic/pyrrolic N species on polyaniline-derived nitrogen-doped mesoporous carbon surface accelerate the dehydrogenation reaction through strong metal–support interactions.^[30] Nevertheless, no research has focused on advanced nitrogen-doped carbon-supported palladium catalysts towards *N*-allylation reactions. Additionally, the effect of the nitrogen-doped support, especially the nitrogen type, still requires further exploration and discussion. Unravelling the nature of interactions between palladium and nitrogen-doped carbon surface is crucial to construct efficient and stable *N*-allylation catalysts.

Herein, we demonstrate new nitrogen-doped graphene nanoshells (N-GNS) that support Pd NPs (Pd/N-GNS) as a superior catalyst for the *N*-allylation reaction. N-GNS was synthesized by a facile hard-template method derived from petroleum asphalt, followed by nitrogen doping with urea as the nitrogen source. The doped nitrogen contents and species could be altered by varying the calcination temperature. Experimental results and DFT calculations reveal strong metal–support interactions between the pyridinic N and palladium species, which impact the growth of Pd NPs on N-GNS, modulate the electronic properties, and promote the adsorption of reactant, thereby significantly boosting the catalytic efficiency for the *N*-allylation reaction. In addition, the Pd/N-GNS catalyst also exhibited excellent stability and could be recycled several times without activity deterioration and metal leaching.

Results and Discussion

Synthesis and characterization of Pd/N-GNS

Pd/N-GNS was prepared through a facile synthetic methodology as shown in Scheme 1. Petroleum asphalt contains a high content of polycyclic aromatic hydrocarbons and is employed as a cost-effective carbon precursor for the synthesis of porous nanoshell-structured supports through a facile hard-template method. First, α -Fe₂O₃ nanoparticles were encapsulated by the viscous petroleum asphalt, which was further carbonized under inert atmosphere. The sacrificial template was removed by acid etching to obtain graphene nanoshells (GNS). Subse-



Scheme 1. Schematic illustration of the preparation procedure for Pd/N-GNS and Pd/GNS.

quently, employing urea as the nitrogen source, N-GNS was prepared by doping nitrogen into GNS. Then, ultra-small Pd NPs were homogeneously deposited onto the N-GNS support to achieve Pd/N-GNS through a mild solvent-growth approach.^[31] As a contrast, Pd/GNS was also prepared by directly anchoring Pd NPs onto GNS₈₀₀, which was obtained by further calcination without addition of urea.

The structure and morphology of the samples were firstly characterized by SEM and TEM. As shown in Figure S1 a (in the Supporting Information), compared with the bulk structure of calcined petroleum asphalt (CPA) under inert atmosphere without α -Fe₂O₃ template, the SEM image of GNS (Figure S1 b in the Supporting Information) exhibits an abundant porous structure, revealing the basic pore-forming role of the nano α -Fe₂O₃ template. According to the TEM image of GNS in Figure 1 a, the dense mesopores show an average diameter of approximately 30 nm, in accordance with the template size. Importantly, high-resolution TEM (HR-TEM) tests clearly present the (002) lattice spacing of carbon, revealing the well-graphitized feature of the carbon nanoshells (Figure 1 a, inset).

This should be attributed to the special activation and catalytic graphitization effect of metallic iron species derived from thermal reduction of α -Fe₂O₃ by carbon.^[32–34] After nitrogen doping, N-GNS₈₀₀ shows only slight differences to GNS₈₀₀ and maintains the porous nanoshell structure (Figure 1 b). Owing to the versatile property induced by nitrogen doping, Pd NPs with uniform small size were well distributed and tightly anchored on the N-GNS₈₀₀ support (Figure 1 d). However, without

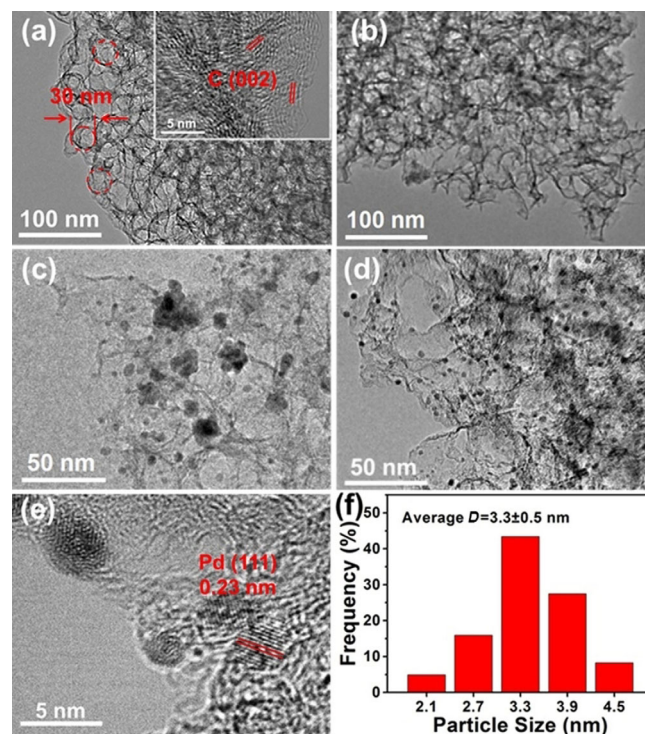


Figure 1. (a) TEM image of GNS and corresponding HR-TEM image (inset). TEM images of (b) N-GNS₈₀₀, (c) Pd/GNS₈₀₀, and (d) Pd/N-GNS₈₀₀. (e) HR-TEM image of Pd/N-GNS₈₀₀ and (f) corresponding palladium particle-size distribution.

nitrogen doping, Pd/N-GNS₈₀₀ suffers from serious agglomeration of Pd NPs, with a wide size distribution and mean diameter of 8.1 nm (Figure 1 c). The HR-TEM image of Pd/N-GNS₈₀₀ shows a well-resolved lattice spacing of 0.23 nm, corresponding to the (111) planes of face-centered cubic metallic palladium (Figure 1 e). Further statistical analysis reveals a narrow palladium size distribution ranging from 2.1 to 4.5 nm, with an average diameter of (3.3 ± 0.5) nm (Figure 1 f). The result indicates that incorporation of nitrogen atoms dramatically changes the properties of the support, which plays a significant role in the growth of Pd NPs. Appropriate nitrogen doping can efficiently decrease the particle size of Pd NPs and favor their good dispersion on the substrate.

The pore features of the samples were investigated by Brunauer–Emmett–Teller (BET) analysis. As shown in Figure S2 a (in the Supporting Information), both N-GNS₈₀₀ and Pd/N-GNS₈₀₀ exhibit a type IV adsorption/desorption isotherm with clear hysteresis loops, suggesting the existence of abundant mesopores, which can also be confirmed by the pore size distribution of N-GNS₈₀₀ and Pd/N-GNS₈₀₀ (Figure S2 b in the Supporting Information). N-GNS₈₀₀ and Pd/N-GNS₈₀₀ show high specific surface areas of 941 and 659 m² g⁻¹, respectively. The decrease should be ascribed to the introduction of Pd NPs, which is supported by the fact that Pd/N-GNS₈₀₀ shows lower pore volume than N-GNS₈₀₀, below 30 nm diameter. The micropores and mesopores provide favorable locations for the deposition of Pd NPs. Moreover, the porous structure and high surface area of Pd/N-GNS₈₀₀ would efficiently facilitate mass transfer of the reactants and products in the reaction process.

XRD was employed to determine the crystal structure of the samples. As seen in Figure 2 a, GNS, N-GNS₈₀₀, and Pd/N-GNS₈₀₀ all present two peaks at approximately 23.8 and 43.3°, which correspond to the (002) and (100) planes of typical amorphous carbon. Compared with GNS, N-GNS₈₀₀ and Pd/N-GNS₈₀₀ show broader and weaker diffraction peaks, indicating a more disordered structure arising from nitrogen doping and Pd deposition. Notably, Pd/N-GNS₈₀₀ exhibits a broad peak at 40.0° and two weak diffraction peaks at 46.5 and 67.9°, which are assigned to the (111), (200), and (220) planes of metallic Pd (JCPDS # 88-2335). The peak intensity indicates the high exposure of (111) crystal planes of the Pd NPs. According

to the Debye–Scherrer equation, the average size of Pd NPs is calculated to be 3.6 nm, which is close to that of the above statistical analysis result. The structural changes of GNS, N-GNS₈₀₀, and Pd/N-GNS₈₀₀ were further characterized by Raman spectroscopy. Figure 2 b illustrates the presence of two peaks at approximately 1350 cm⁻¹ (D band), corresponding to structure defects, and 1595 cm⁻¹ (G band), associated with the stretching vibration mode of graphite crystals. The peak intensity ratios (*I*_D/*I*_G) of N-GNS₈₀₀ and Pd/N-GNS₈₀₀ are 1.06 and 1.04, respectively, which is relatively higher than that of GNS (*I*_D/*I*_G = 0.93), revealing the formation of abundant defects after nitrogen incorporation. The similar *I*_D/*I*_G value of N-GNS₈₀₀ and Pd/N-GNS₈₀₀ suggests no significant structural change after Pd deposition.

To further examine the surface chemistry of the composites, X-ray photoelectron spectroscopy (XPS) analysis was conducted. Compared with GNS, the full-range XPS spectra of N-GNS₈₀₀ and Pd/N-GNS₈₀₀ show additional N and Pd signals in addition to C and O in the samples (Figure 3 a). The high-resolution C 1s

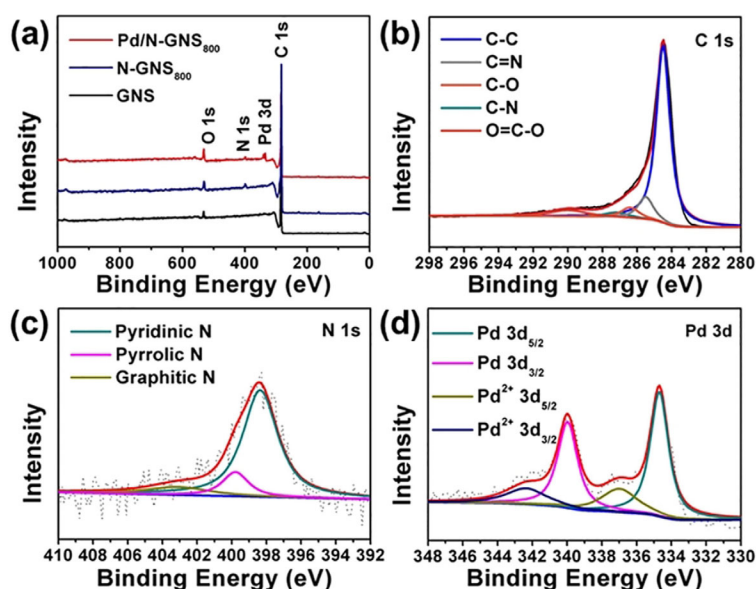


Figure 3. (a) Full-range XPS survey spectra of GNS, N-GNS₈₀₀, and Pd/N-GNS₈₀₀. (b) C 1s, (c) N 1s, and (d) Pd 3d high-resolution spectra of Pd/N-GNS₈₀₀.

XPS spectrum of Pd/N-GNS₈₀₀ reveals the presence of C=N and C–N bonds at 285.7 and 287.2 eV, respectively, suggesting successful nitrogen doping into the carbon skeleton (Figure 3 b). The high-resolution N 1s XPS spectrum is split into peaks at 398.4, 399.8, and 402.5 eV, attributed to pyridinic, pyrrolic, and graphitic N species, respectively (Figure 3 c). Among them, pyridinic N is the main doping type, which constitutes 76.7% of the total nitrogen atoms. Additionally, four major contributions can be identified from the Pd 3d spectra of Pd/N-GNS₈₀₀ (Figure 3 d) and Pd/GNS₈₀₀ (Figure S3 in the Supporting Information), simultaneously. For Pd/N-GNS₈₀₀, Pd 3d_{5/2} and 3d_{3/2} peaks observed at 334.7 and 339.9 eV correspond to metallic Pd,

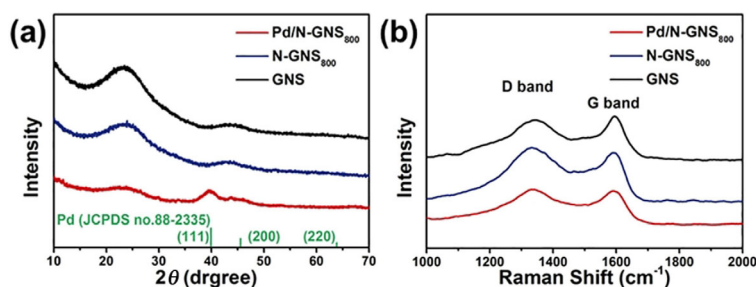
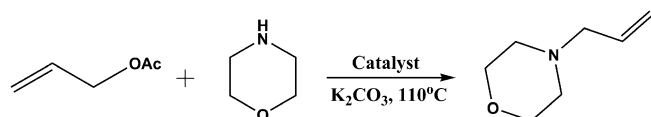


Figure 2. (a) XRD and (b) Raman patterns of GNS, N-GNS₈₀₀, and Pd/N-GNS₈₀₀.

whereas the 337.0 and 342.2 eV peaks indicate the existence of Pd²⁺ species. The Pd⁰ percentage in fresh Pd/N-GNS₈₀₀ is estimated to be 80.5% (Figure 3d), much higher than Pd/GNS₈₀₀ (22.9%, Figure S3 in the Supporting Information), implying that the nitrogen-doped support can efficiently promote the reduction of Pd²⁺ to Pd⁰ catalytic species. Notably, compared with Pd/GNS₈₀₀, the Pd 3d_{5/2} peak of Pd/N-GNS₈₀₀ shows a clear shift to lower binding energy from 335.0 to 334.7 eV. The phenomenon indicates a considerable charge transfer from the nitrogen-doped support to Pd species, implying a strong surface–metal interaction.^[35,36] The electron donation effect of the nitrogen-doped support would increase the electronic density around palladium and further facilitate the formation of Pd NPs.^[37] The nitrogen-doping content in Pd/N-GNS₈₀₀ is measured to be 3.6 wt% by elemental analysis (EA), and the palladium amount is evaluated to be 6.4 wt% by inductively coupled plasma optical emission spectrometry (ICP-OES).

Catalytic *N*-allylation reaction

N-Allylation of morpholine with allyl acetate was examined as a model reaction to evaluate the catalytic performance of the catalysts. The reaction was conducted at 110 °C by using anhydrous K₂CO₃ as an external base (Scheme 2). Excess morpholine was added, acting as both reactant and solvent. The catalytic results are summarized in Table 1. The reaction hardly proceeded with no catalyst (entry 1), indicating the necessity of an efficient catalyst. GNS and N-GNS₈₀₀ both resulted in poor conversion of less than 5% (entries 2 and 3), whereas a sharp increase was observed by using intercalated Pd NPs, clarifying the cata-



Scheme 2. *N*-Allylation of morpholine with allyl acetate.

Entry	Catalyst	<i>t</i> [h]	Conv. [%]	Sel. [%]	Final TOF [h ⁻¹]
1	blank	1.5	0.9	–	–
2	GNS	1.5	1.5	–	–
3	N-GNS ₈₀₀	1.5	2.1	–	–
4	Pd/GNS ₈₀₀	1.5	15.6	≈ 100	8.0
5	Pd/N-GNS ₈₀₀	1.0	65.4	≈ 100	54.4
6	Pd/N-GNS ₈₀₀	1.5	92.2	≈ 100	51.2
7	Pd/N-GNS ₇₀₀	1.5	59.1	≈ 100	32.8
8	Pd/N-GNS ₉₀₀	1.5	47.2	≈ 100	26.2
9	Pd/N-GNS ₁₀₀₀	1.5	35.8	≈ 100	19.9
10	Pd/C ^[b]	1.5	31.4	≈ 100	17.4
11	Pd/C + N-GNS ₈₀₀ ^[c]	1.5	26.3	≈ 100	14.6
12	Pd/N-GNS ^[d]	1.5	90.4	≈ 100	50.2

[a] Reaction conditions: allyl acetate (1.0 mmol), catalyst (0.012 mmol Pd), morpholine (5.0 mL), K₂CO₃ (2 mmol), 110 °C, Ar atmosphere. Final TOF = mol_{converted}/mol_{active sites}⁻¹/t. [b] Commercial Pd/C catalyst (12.8 mg, 0.012 mmol Pd). [c] Commercial Pd/C catalyst (12.8 mg) and N-GNS (18.7 mg). [d] After being reused for four cycles.

lytic efficiency of palladium towards the *N*-allylation reaction. Particularly, Pd/N-GNS₈₀₀ delivered a high yield of 65.2 and 92.2% within 1.0 h and 1.5 h, respectively, the catalytic activity of which is about 6-fold higher than Pd/GNS₈₀₀ (entries 4–6), revealing significant enhancement of the catalytic activity arising from nitrogen doping. Pd/N-GNS₇₀₀, Pd/N-GNS₉₀₀, and Pd/N-GNS₁₀₀₀ afforded conversions of 59.1, 47.2, and 35.8%, respectively. The distinct activity of Pd/N-GNS catalysts prepared at different temperatures suggests the significant influence of the support on their catalytic performance. As a control, a commercial Pd/C catalyst only obtained a conversion of 31.4% after 1.5 h (entry 10), which is considerably lower than Pd/N-GNS₈₀₀. A wider comparison with reported catalysts further demonstrates the superior catalytic efficiency of the Pd/GNS₈₀₀ catalyst (Table S1 in the Supporting Information). To illustrate the promoted effect of nitrogen-doped supports, N-GNS₈₀₀ was mixed with commercial Pd/C catalyst as a promoter. Unexpectedly, the Pd/C + N-GNS₈₀₀ composite only resulted in a slightly lower yield (26.3%) than pristine Pd/C catalyst (entry 11 vs. 10). Thus, N-GNS₈₀₀ cannot promote the catalytic efficiency of the Pd/C catalyst, or even leads to increased transfer resistance during the reaction process. This result demonstrates that the superior catalytic performance of Pd/N-GNS₈₀₀ is attributed to the strong interaction between the nitrogen-doped support and palladium active species. Moreover, the Pd/N-GNS₈₀₀ catalyst showed excellent reusability and could be recycled for at least four cycles without significant deterioration in catalytic activity (entry 12).

The robust stability of Pd/N-GNS₈₀₀ was further confirmed by hot-filtration experiments and TEM tests. As shown in Figure 4a, after hot filtration of solid Pd/GNS₈₀₀ (conversion of

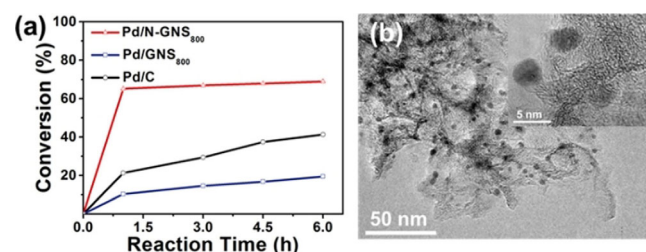


Figure 4. (a) Hot-filtration tests of Pd/C, Pd/GNS₈₀₀, and Pd/N-GNS₈₀₀. (b) TEM and HR-TEM (inset) images of Pd/N-GNS₈₀₀ after being reused for four cycles.

10.3%) and commercial Pd/C catalysts (conversion of 21.2%) at 1.0 h, the reaction continued to proceed and resulted in a conversion of 19.4% and 41.4% after 5 h, respectively, suggesting leaching of active species into the solvent. For Pd/N-GNS₈₀₀ (conversion of 65.2%), no further reaction proceeded in the filtrate, which implies that the catalytic reaction occurred at the solid surface. Additionally, it is found that the TEM image of Pd/N-GNS₈₀₀ after recycling showed similar features as fresh Pd/N-GNS₈₀₀. Pd NPs with an average diameter of 3.6 nm were homogeneously dispersed on the carbon-based substrate, with no significant aggregation (Figure 4b and inset). These results demonstrate the excellent stability of the prepared catalyst. Therefore, nitrogen doping not only efficiently promotes the

catalytic activity for the *N*-allylation reaction, but also drastically reinforces the durability of the catalyst.

Considering the superior catalytic efficiency of Pd/N-GNS₈₀₀, further studies were performed to give better insight into the nature of the catalytic properties. Typically, the pore structure of the catalyst greatly influences its catalytic performance. Thus, further BET analyses of Pd/N-GNS₇₀₀, Pd/N-GNS₉₀₀, and Pd/N-GNS₁₀₀₀ were performed and are shown in Figure S4 (in the Supporting Information). Similar to Pd/N-GNS₈₀₀ in Figure S2 (in the Supporting Information), all samples exhibit a type IV adsorption/desorption isotherm and possess abundant mesopores. Pd/N-GNS₇₀₀, Pd/N-GNS₈₀₀, Pd/N-GNS₉₀₀, and Pd/N-GNS₁₀₀₀ show high specific surface areas of 664, 659, 929, and 976 m² g⁻¹ with corresponding final turnover frequencies (TOFs) of 51.2, 32.8, 26.2, and 19.9, respectively (Figure S5 in the Supporting Information). The results suggest that surface area and pore features are not the crucial factor to determine the catalytic properties. A further study of the XPS results of Pd/N-GNS catalysts revealed that the doped nitrogen contents and species can be readily altered by varying the calcination temperature, which further affects the deposition of Pd NPs (Figure S6 in the Supporting Information). Figure 5 exhibits the

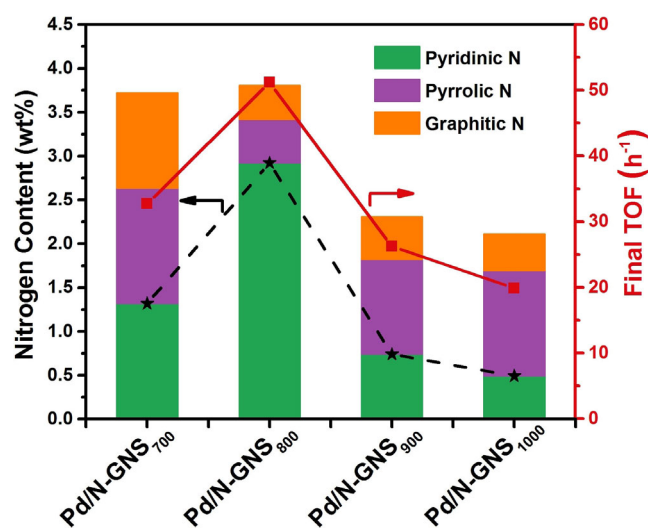


Figure 5. Nitrogen content of each type of N species of Pd/N-GNS₇₀₀, Pd/N-GNS₈₀₀, Pd/N-GNS₉₀₀, and Pd/N-GNS₁₀₀₀, and corresponding catalytic final TOF.

nitrogen composition and corresponding catalytic performance of the Pd/N-GNS catalysts. It is worth noting that Pd/N-GNS₇₀₀ and Pd/N-GNS₈₀₀ possess similar total nitrogen contents, whereas Pd/N-GNS₈₀₀ shows nearly 1.8-fold activity compared with Pd/N-GNS₇₀₀, which implies the distinct roles of different types of nitrogen species. With the increase of calcination temperature, the nitrogen doping content decreases gradually, resulting in inferior catalytic performance of Pd/N-GNS₉₀₀ and Pd/N-GNS₁₀₀₀. Further investigation illustrates a significant relationship between the nitrogen types and their catalytic efficiency. As can be seen, the black dotted line presents the pyridinic N contents of the Pd/N-GNS samples, a trend that corresponds

well with the catalytic activity (red line). The linear correlation reveals that pyridinic N is responsible for the superior catalytic properties of the Pd/N-GNS catalysts. Among the catalysts, Pd/N-GNS₈₀₀ shows the highest pyridinic N content (2.8 wt%) and percentage (76.7%), thereby affording the best catalytic performance.

Theoretical calculations and mechanism studies

To better unravel the intrinsic interactions between the palladium and nitrogen species on the N-GNS support, the adsorption interaction was further studied by DFT calculations. To simplify the calculation process, a palladium cluster containing four atoms was used as a model active substance, located on graphene, graphitic N, pyridinic N, and pyrrolic N models of carbon-based substrates. Detailed configurations and the adsorption energy (E_{ads}) at each site are shown in Figure 6. The

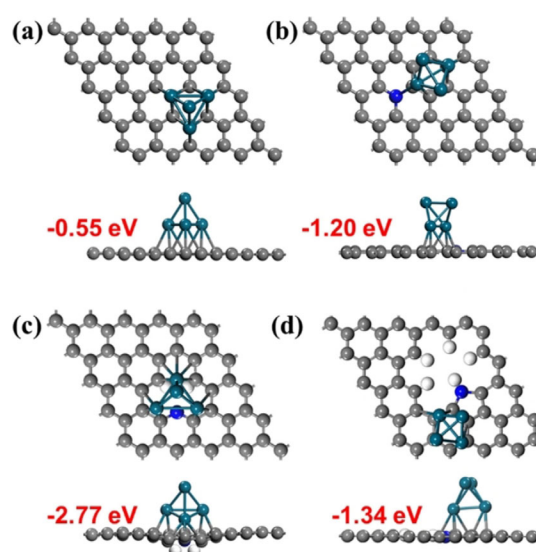
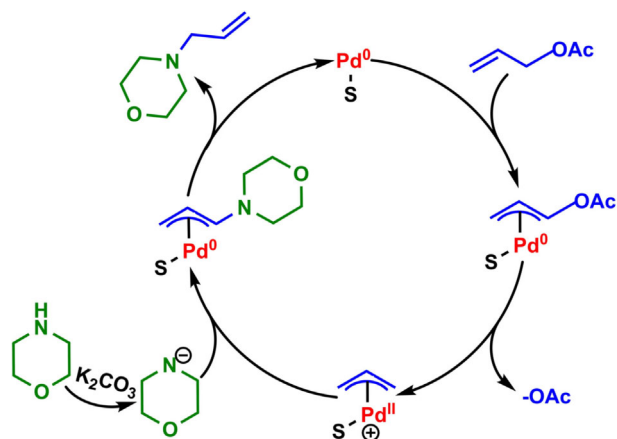


Figure 6. Top and side views for Pd cluster adsorption on carbon-based models of (a) graphene, (b) graphitic N, (c) pyridinic N, and (d) pyrrolic N. The grey, blue, white, and green balls stand for carbon, nitrogen, hydrogen, and palladium atoms, respectively.

E_{ads} values of the four models are calculated to be -0.55 , -1.20 , -2.77 , and -1.34 eV, respectively. Among them, pyridinic N exhibits by far the highest E_{ads} , nearly five times that of the pristine graphene model. Combined with the XPS results above, the results reveal the extremely strong electronic and chemical interactions between pyridinic N and palladium species.^[38] Considering pyridinic N usually has a lone pair of electrons, nitrogen functionalities are expected to be more effective in retaining and inducing the growth Pd NPs, and thus lead to a dramatic enhancement in the catalytic performance.^[29,39] Additionally, because transfer of amines to the active sites is a critical step for C–N coupling processes,^[40] the E_{ads} of morpholine onto the four different models was further calculated to evaluate the adsorption ability of the reactant. It is found that pyridinic N exhibits the largest E_{ads} among the four models (Figure S7 in the Supporting Information). There-

fore, the pyridinic N-supported palladium catalyst can also enhance the transfer efficiency of morpholine in the reaction process, which is favorable for the smooth proceeding of the reaction.

Scheme 3 illustrates the reaction mechanism invoked for *N*-allylation over the Pd/N-GNS catalyst. S stands for the nitrogen-doped support (N-GNS), acting as special ligands to coordinate with Pd active species and to adjust their electronic



Scheme 3. Proposed reaction mechanism for the *N*-allylation reaction. S represents the nitrogen-doped support anchoring Pd active species.

properties in the reaction cycle. At the beginning of the reaction cycle, the palladium(0) coordinates to the alkene and forms a π -allyl palladium(0) complex. Next, oxidative addition occurs in which the leaving group is expelled with inversion of configuration and a π -allyl palladium(II) is created. The base-activated nucleophile then adds to the allyl group, regenerating the π -allyl palladium(0) complex.^[41–43] At the completion of the reaction, palladium detaches from the allylated product and starts a subsequent catalytic cycle. According to the obtained experimental and theoretical results, the pyridinic N-doped support increases the electronic density around palladium, which would promote the oxidative addition of the palladium active center to allyl acetate. Additionally, the enhanced adsorption ability of morpholine onto the catalytic sites causes smooth progress of the reaction cycle, promoting the intrinsic catalytic activity. Additionally, the strong metal–support interactions between pyridinic N and palladium species can impact the growth of Pd NPs, which results in tight deposition, smaller particle size, uniform dispersion, and exposure of more effective active sites. Moreover, the nanoshell-structured N-GNS support with high surface area could prevent the leaching of Pd NPs and facilitate mass transfer of the reactants and products in the reaction process.^[44–46] Therefore, considering the above merits, a highly efficient and stable palladium catalyst for *N*-allylation reaction is achieved.

Conclusions

We successfully synthesized pyridinic nitrogen-doped graphene nanoshells to support Pd NPs as a highly efficient and

recyclable catalyst toward the *N*-allylation reaction. Introduction of nitrogen led to 6-fold enhancement of the catalytic activity. The catalyst also showed robust stability and could be recycled several times without activity deterioration and metal leaching. The promoted catalytic performance is caused by strong metal–support interactions between the pyridinic N and palladium species on the support, which can efficiently downsize the Pd NPs, modulate the electronic density of palladium, and accelerate the adsorption of the reactant, thereby significantly boosting the catalytic efficiency for the *N*-allylation reaction. These results demonstrate that pyridinic nitrogen-doped carbon matrixes are promising substrates for constructing advanced palladium catalysts for *N*-allylation reactions and other chemical transformations.

Experimental Section

Materials

Petroleum asphalt was obtained from the China National Offshore Oil Corporation (17.63 wt% saturates, 31.13 wt% aromatics, 38.21 wt% resins, and 6.40% asphaltenes). α -Fe₂O₃ nanoparticles (30 nm), methanol (99.9%), allyl acetate (99%), morpholine (99%), Pd/C catalyst (10 wt% Pd), hydrochloric acid (36–38 wt%), and potassium carbonate (99%) were purchased from Aladdin Reagent Co. Urea (99%) and palladium acetate (Pd 46–48%) was purchased from Macklin Biochemical Co. All reagents were used as received from commercial suppliers without further purification.

Preparation of GNS and N-GNS

Petroleum asphalt (1 g) was dissolved in toluene (50 mL) and stirred for 10 min. Then, α -Fe₂O₃ nanoparticles (4 g) were added into the solution with vigorous stirring and formed a uniform suspension. Brown powder was produced by distillation under reduced pressure, which was further carbonized at 800 °C for 1 h under N₂ atmosphere. The resulting sample was then etched with 2 M HCl at 90 °C for 8 h to remove the residual template. After filtration and washing with deionized water until neutral, followed by drying at 80 °C overnight, graphene nanoshells (GNS) were finally observed. As a control, CPA was also prepared by calcining petroleum asphalt at 800 °C for 1 h under N₂ atmosphere without α -Fe₂O₃ template. Subsequently, GNS was mixed with urea at a mass ratio of 1:5 and calcined for 2 h under N₂ atmosphere to achieve N-GNS. To alter the nitrogen contents and species, the calcination temperatures were set as 700, 800, 900, and 1000 °C to obtain N-GNS₇₀₀, N-GNS₈₀₀, N-GNS₉₀₀, and N-GNS₁₀₀₀, respectively. For comparison, GNS was further calcined at 800 °C for 2 h under N₂ atmosphere without the addition of urea and was denoted as GNS₈₀₀.

Synthesis of Pd/N-GNS

The synthesis of Pd/N-GNS was performed as follows: N-GNS (50 mg) was dispersed in methanol (10 mL) with intense stirring, followed by addition of Pd(OAc)₂ (7.5 mg) into the suspension. After ultrasonication for 10 min, the mixture was stirred at 40 °C for 5 h. Finally, the resulting catalysts were collected by filtration and washed with deionized water three times, followed by drying in a vacuum oven at 80 °C for 10 h. According to the different N-GNS supports, the Pd/N-GNS catalysts were denoted as Pd/N-GNS₇₀₀, Pd/N-GNS₈₀₀, Pd/N-GNS₉₀₀, and Pd/N-GNS₁₀₀₀, respectively. As a con-

trol, Pd/GNS₈₀₀ was produced by the same method apart from using GNS₈₀₀ as the pristine support.

Characterization

SEM images (Hitachi S-4800) and TEM images (JEM-2100F) were utilized to observe the morphology of the samples. The crystal structure was characterized by XRD (X'Pert PRO MPD) with CuK_α radiation (1.518 Å). Raman analysis was conducted by using a Jobin-Yvon Labram-010 Raman spectrometer. The elemental composition and chemical bonding were studied by XPS with a MgK_α radiation (1486.6 eV) monochromatic X-ray source (Thermo Scientific Escalab 250XI). BET was employed to measure the specific surface area and pore properties. The palladium contents were detected by ICP-OES (Vista-MPX). The catalytic results were determined by GC (BF-2002) with a flame-ionization detector.

General procedure for the N-allylation reaction

The catalytic reactions were conducted in a 10 mL sealed Schlenk tube. Generally, Pd/N-GNS (0.012 mmol Pd species) and K₂CO₃ (2.0 mmol, 279.3 mg) were dispersed in morpholine (5 mL). Subsequently, allyl acetate (1.0 mmol, 101.1 mg) was added into the suspension. After degassing with Ar three times, the mixture was heated to 110 °C with an oil bath and reacted for 1.5 h. After cooling to room temperature, a sample was taken from the mixture for GC analysis. For the control experiments, catalysts containing the same amount of palladium species (0.012 mmol) were used under the above reaction conditions. Repeated experiments were performed to obtain averaged catalytic data. After the reaction, the catalyst was recovered from the reaction system by filtration and washed with ethanol three times. The recycled catalyst was dried in a vacuum oven and reused in the sequential cycles. For the hot-filtration experiments, the reactions were conducted under the same reaction conditions as above. The catalyst was removed quickly by filtration after reacting for 1 h, and the filtrate was transferred to a clean Schlenk tube containing K₂CO₃ (2.0 mmol). After degassing with Ar three times, the mixture continued to react for another 5 h.

DFT calculations

The DFT calculations for the adsorption of Pd clusters on different supports and adsorption of morpholine (MOR) on palladium-decorated carbon (Pd-C) catalysts were performed by using the Vienna Ab-initio Simulation Package (VASP). The interaction between the valence electrons and the core was described by projected augmented wave potentials. The exchange correlation energy was calculated with the generalized gradient approximation (GGA) as parameterized by Perdew et al. based on the Perdew–Burke–Ernzerhof (PBE) functional.^[47] The Kohn–Sham orbitals were expanded in a plane wave basis set with a kinetic cutoff energy of 400 eV. Based on the lattice size, the Monkhorst–Pack meshes of 2×2×2 k-point samplings in the surface Brillouin zones were used for the graphite surfaces with unit cells of 5×5,^[48] 3×3×3 for the Pd cluster, 2×2×2 for the Pd-C structure, and 1×1×1 for the MOR-Pd-C structure. All structures were fully relaxed. A vacuum layer of 15 Å along the direction of the surface normal was used to avoid periodic interactions. All calculations were spin-polarized and the optimization was converged until the forces on each atom were below 0.03 eV Å⁻¹ and the total energy differences were less than 10⁻⁴ eV. The adsorption energy of A (i.e., Pd cluster or MOR) was calculated

by using Equation (1):

$$E_{\text{ads}} = E_{\text{A/surface}} - E_{\text{A}} - E_{\text{surface}} \quad (1)$$

in which $E_{\text{A/surface}}$ is the total energy of the surface adsorbed with the Pd cluster or MOR, E_{surface} is the total energy of the clean surface, and E_{A} is the total energy of Pd cluster or MOR.

Acknowledgements

This work was financially supported by the National Natural Science Foundation of China (No. 51572296, U1662113, 21606254); the Fundamental Research Fund for the Central Universities (No. 18CX02015A, 15CX08005A); the CAS Key Laboratory of Carbon Materials (No. KLCMKFJJ1705); the Shandong Provincial Natural Science Foundation (No. ZR2016BB18); the Financial Support from Taishan Scholar Project; and the Scientific Research and Technology Development Project of Petrochina Co., LTD (2016B-2004(GF)).

Conflict of interest

The authors declare no conflict of interest.

Keywords: doping · graphene nanoshells · N-allylation · palladium · pyridinic N

- [1] Y. Park, Y. Kim, S. Chang, *Chem. Rev.* **2017**, *117*, 9247–9301.
- [2] F. Panahi, F. Daneshgar, F. Haghghi, A. Khalafi-Nezhad, *J. Organomet. Chem.* **2017**, *851*, 210–217.
- [3] S. R. Vemula, D. Kumar, G. R. Cook, *ACS Catal.* **2016**, *6*, 5295–5301.
- [4] R. B. N. Baig, B. R. Vaddula, M. A. Gonzalez, R. S. Varma, *RSC Adv.* **2014**, *4*, 9103–9106.
- [5] P. Ruiz-Castillo, S. L. Buchwald, *Chem. Rev.* **2016**, *116*, 12564–12649.
- [6] B. Lu, B. Feng, H. Ye, J. R. Chen, W. J. Xiao, *Org. Lett.* **2018**, *20*, 3473–3476.
- [7] D. Yu, F. Zhou, D. S. W. Lim, H. Su, Y. Zhang, *ChemSusChem* **2017**, *10*, 836–841.
- [8] G. Meng, P. Lei, M. Szostak, *Org. Lett.* **2017**, *19*, 2158–2161.
- [9] K. Motokura, K. Saitoh, H. Noda, W.-J. Chun, A. Miyaji, S. Yamaguchi, T. Baba, *Catal. Sci. Technol.* **2016**, *6*, 5380–5388.
- [10] P.-F. Vittoz, H. El Siblani, A. Bruma, B. Rigaud, X. Sauvage, C. Fernandez, A. Vicente, N. Barrier, S. Malo, J. Levillain, A.-C. Gaumont, I. Dez, *ACS Sustainable Chem. Eng.* **2018**, *6*, 5192–5197.
- [11] W. Zhou, B. Zou, W. Zhang, D. Tian, W. Huang, F. Huo, *Nanoscale* **2015**, *7*, 8720–8724.
- [12] H. Tang, Y. Su, Y. Guo, L. Zhang, T. Li, K. Zang, F. Liu, L. Li, J. Luo, B. Qiao, J. Wang, *Chem. Sci.* **2018**, *9*, 6679–6684.
- [13] H. Mao, Y. Shen, Q. Zhang, M. Ulaganathan, S. Zhao, Y. Yang, H. H. Hng, *Carbon* **2016**, *96*, 75–82.
- [14] S. Crossley, J. Faria, M. Shen, D. E. Resasco, *Science* **2010**, *327*, 68–72.
- [15] X. Xu, Y. Li, Y. Gong, P. Zhang, H. Li, Y. Wang, *J. Am. Chem. Soc.* **2012**, *134*, 16987–16990.
- [16] J. Zhang, S. Lu, Y. Xiang, P. K. Shen, J. Liu, S. P. Jiang, *ChemSusChem* **2015**, *8*, 2956–2966.
- [17] C.-H. Pélisson, T. Nakanishi, Y. Zhu, K. Morisato, T. Kamei, A. Maeno, H. Kaji, S. Muroyama, M. Tafu, K. Kanamori, T. Shimada, K. Nakanishi, *ACS Appl. Mater. Interfaces* **2017**, *9*, 406–412.
- [18] K. Koh, M. Jeon, C. W. Yoon, T. Asefa, *J. Mater. Chem. A* **2017**, *5*, 16150–16161.
- [19] T. Ishida, K. Kume, K. Kinjo, T. Honma, K. Nakada, H. Ohashi, T. Yokoyama, A. Hamasaki, H. Murayama, Y. Izawa, M. Utsunomiya, M. Tokunaga, *ChemSusChem* **2016**, *9*, 3441–3447.

- [20] M. Ye, J. Gong, Y. Lai, C. Lin, Z. Lin, *J. Am. Chem. Soc.* **2012**, *134*, 15720–15723.
- [21] M. Hu, S. Zhao, S. Liu, C. Chen, W. Chen, W. Zhu, C. Liang, W. C. Cheong, Y. Wang, Y. Yu, Q. Peng, K. Zhou, J. Li, Y. Li, *Adv. Mater.* **2018**, *30*, 1801878.
- [22] V. Georgakilas, J. A. Perman, J. Tucek, R. Zboril, *Chem. Rev.* **2015**, *115*, 4744–4822.
- [23] R. W. Lodge, G. A. Rance, M. W. Fay, A. N. Khlobystov, *Nanoscale* **2018**, *10*, 19046–19051.
- [24] Z. Li, J. Liu, C. Xia, F. Li, *ACS Catal.* **2013**, *3*, 2440–2448.
- [25] G. Ji, Y. Duan, S. Zhang, B. Fei, X. Chen, Y. Yang, *ChemSusChem* **2017**, *10*, 3427–3434.
- [26] X. Duan, J. Liu, J. Hao, L. Wu, B. He, Y. Qiu, J. Zhang, Z. He, J. Xi, S. Wang, *Carbon* **2018**, *130*, 806–813.
- [27] Y. Cao, S. Mao, M. Li, Y. Chen, Y. Wang, *ACS Catal.* **2017**, *7*, 8090–8112.
- [28] O. Y. Podyacheva, D. A. Bulushev, A. N. Suboch, D. A. Svintsitskiy, A. S. Lisitsyn, E. Modin, A. Chuvilin, E. Y. Gerasimov, V. I. Sobolev, V. N. Parmon, *ChemSusChem* **2018**, *11*, 3724–3727.
- [29] Q. Y. Bi, J. D. Lin, Y. M. Liu, H. Y. He, F. Q. Huang, Y. Cao, *Angew. Chem. Int. Ed.* **2016**, *55*, 11849–11853; *Angew. Chem.* **2016**, *128*, 12028–12032.
- [30] K. Koh, M. Jeon, D. M. Chevrier, P. Zhang, C. W. Yoon, T. Asefa, *Appl. Catal. B* **2017**, *203*, 820–828.
- [31] Q. L. Zhu, N. Tsumori, Q. Xu, *J. Am. Chem. Soc.* **2015**, *137*, 11743–11748.
- [32] W. Lian, H. Song, X. Chen, L. Li, J. Huo, M. Zhao, G. Wang, *Carbon* **2008**, *46*, 525–530.
- [33] N. P. Wickramaratne, V. S. Perera, B.-W. Park, M. Gao, G. W. McGimpsey, S. D. Huang, M. Jaroniec, *Chem. Mater.* **2013**, *25*, 2803–2811.
- [34] M. Xie, J. Yang, J. Liang, X. Guo, W. Ding, *Carbon* **2014**, *77*, 215–225.
- [35] F. Wang, J. Xu, X. Shao, X. Su, Y. Huang, T. Zhang, *ChemSusChem* **2016**, *9*, 246–251.
- [36] Y. Tong, G. Xue, H. Wang, M. Liu, J. Wang, C. Hao, X. Zhang, D. Wang, X. Shi, W. Liu, G. Li, Z. Tang, *Nanoscale* **2018**, *10*, 16425–16430.
- [37] Y.-H. Qin, Z.-Y. Xiong, J. Ma, L. Yang, Z. Wu, W. Feng, T.-L. Wang, W.-G. Wang, C.-W. Wang, *Int. J. Hydrogen Energy* **2017**, *42*, 1103–1112.
- [38] X. Duan, M. Xiao, S. Liang, Z. Zhang, Y. Zeng, J. Xi, S. Wang, *Carbon* **2017**, *119*, 326–331.
- [39] P. Zhang, Y. Gong, H. Li, Z. Chen, Y. Wang, *Nat. Commun.* **2013**, *4*, 1593.
- [40] J. M. Dennis, N. A. White, R. Y. Liu, S. L. Buchwald, *J. Am. Chem. Soc.* **2018**, *140*, 4721–4725.
- [41] L. A. Evans, N. Fey, J. N. Harvey, D. Hose, G. C. Lloyd-Jones, P. Murray, A. G. Orpen, R. Osborne, G. J. J. Owen-Smith, M. Purdie, *J. Am. Chem. Soc.* **2008**, *130*, 14471–14473.
- [42] Q. Zhao, Y. Zhu, Z. Sun, Y. Li, G. Zhang, F. Zhang, X. Fan, *J. Mater. Chem. A* **2015**, *3*, 2609–2616.
- [43] N. Kihara, S. Motoda, T. Yokozawa, T. Takata, *Org. Lett.* **2005**, *7*, 1199–1202.
- [44] C. Li, H. Xu, Y. Kido, Y. Yoneyama, Y. Suehiro, N. Tsubaki, *ChemSusChem* **2012**, *5*, 862–866.
- [45] G. Yang, N. Tsubaki, J. Shamoto, Y. Yoneyama, Y. Zhang, *J. Am. Chem. Soc.* **2010**, *132*, 8129–8136.
- [46] Q. Lin, Q. Zhang, G. Yang, Q. Chen, J. Li, Q. Wei, Y. Tan, H. Wan, N. Tsubaki, *J. Catal.* **2016**, *344*, 378–388.
- [47] J. P. Perdew, K. Burke, M. Ernzerhof, *Phys. Rev. Lett.* **1996**, *77*, 3865–3868.
- [48] L. Yu, X. Pan, X. Cao, P. Hu, X. Bao, *J. Catal.* **2011**, *282*, 183–190.

Manuscript received: November 4, 2018

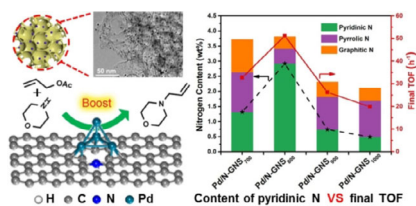
Revised manuscript received: December 15, 2018

Accepted manuscript online: January 2, 2019

Version of record online: ■■■■■ 0000

FULL PAPERS

Nitrogen-doped graphene nanoshells supporting palladium nanoparticles (Pd/N-GNS) have been developed as a superior catalyst for the *N*-allylation reaction. Experimental results and DFT calculations reveal strong metal-support interactions between the pyridinic N and palladium species, which significantly boost the catalytic efficiency and stability of the catalyst.



X. X. Li, Q. S. Zhao,* X. Feng, L. Pan,
Z. Z. Wu, X. C. Wu, T. W. Ma, J. L. Liu,
Y. Y. Pan, Y. Song, M. B. Wu*



Pyridinic Nitrogen-Doped Graphene Nanoshells Boost the Catalytic Efficiency of Palladium Nanoparticles for the *N*-Allylation Reaction

